Materials Science & Engineering C 105 (2019) 110072

Contents lists available at ScienceDirect

Materials Science & Engineering C

journal homepage: www.elsevier.com/locate/msec

Preparation of bioactive hydroxyapatite@halloysite and its effect on MC3T3-E1 osteogenic differentiation of chitosan film

Jingqi Zheng, Fan Wu, Hong Li, Mingxian Liu*

Department of Materials Science and Engineering, Jinan University, Guangzhou 510632, People's Republic of China

ARTICLE INFO

Keywords:
Halloysite
Hydroxyapatite
Osteogenic differentiation
MC3T3-E1

ABSTRACT

Halloysite nanotubes (HNTs) are widely used in biomedical field due to their special tubular structure and high reinforcing ability, while hydroxyapatite (HAP) is generally used in tissue engineering owing to its excellent biocompatibility and biological activity. In this work, hydroxyapatite@halloysite nanotubes(HAP@HNTs) hybrid was synthesized via a facial hydrothermal reaction process. The morphology, particle size, specific surface area, and chemical composition of the hybrid were thoroughly characterized by different techniques. Rod-like HAP nanoparticles can be anchored on the outer surface of the clay tubes, which lead to a maximum increase of 4.7 m^2/g in the specific surface area of HAP@HNTs over that of HNTs. HAP nanoparticles have little effect on the pores of HNTs, but diffraction peak strength of HNTs is covered by the HAP crystals. HAP@HNTs exhibit improved cytocompatibility and possess osteogenic differentiation ability towards MC3T3-E1 preosteoblasts. Chitosan/HAP@HNTs composite films were then prepared by doping of HAP@HNTs into chitosan by solution mixing. HAP@HNTs can serve as a functional phase which enhances mechanical properties of chitosan films and osteogenic differentiation of MC3T3-E1 cells. This work provides a facial synthesis routine of bioactive HAP@HNTs, which combines the osteogenic activity of HAP and the good mechanical properties of HNTs. HAP@HNTs can be used a novel bone regeneration biomaterial as local delivery systems with improved osteoinductive properties.

1. Introduction

As a kind of natural clay mineral, halloysite nanotubes (HNTs), of which chemical formula is $Al_2Si_2O_5(OH)_4{\cdot}nH_2O$, are aluminosilicate nanomaterials [1]. Although elemental composition of halloysite is similar to kaolin, unlike the flaky kaolin, HNTs have a uniquely tubular structure with an outer diameter about 50 nm, an inner diameter 10–15 nm and a tube length between 100 and 1500 nm. Generally, HNTs are added to polymer materials as mechanical enhancing materials. For example, the mechanical properties of PLLA-based nanofiber scaffolds with adding HNTs and bio-composite films composed of chitosan and HNTs are improved [2,3]. In addition, HNTs as drug carriers have significant applications for biomedical field on account of their unique properties such as the nanoscale tubular structure, the controllable surfactant sites and the stability of HNTs under thermal or acid/base treatments [4]. So far, HNTs are able to be used as loading and control-release of multifarious substances which include inorganic salts, simple organic molecules and biochemical molecules with high molecular mass [5–7]. Folic acid-modified HNTs as a carrier of doxorubicin can be designed for drug-specific targeted release towards breast tumor [8]. HNTs modified by cationic polymer can also be used as gene carriers for intracellular delivery of DNA or SiRNA [9]. HNTs have potential applications for controlled delivery systems of nanoformulations which could be designed to supply longer drug release time [10–12]. HNTs loading substances are added to polymer matrix which can be available as drug-loaded tissue engineering scaffolds and antibacterial dressings [13–15]. Moreover, HNTs are used to construct different patterns by self-assembly to capture tumor cells [16].

Raw HNTs have good biocompatibility and very low toxicity, which has been proved both *in vitro* and *in vivo* experiments. For instance, the *in vivo* experiments of HNTs using the animal models such as zebra fish, *Caenorhabditis elegans* and mice show that they are biosafety [17–19]. However, for some special applications in biomaterials, the surface of HNTs can be modified to ensuring some functions such as antibacterial property, long-term cycling stability, and tumor targeting. Coating with polymers on HNTs can enhance the biological stability and safety *in vivo*. Paola et al. coated polyethylene glycol (PEG) on the surface of HNTs and demonstrated that the biocompatibility of PEG-coated HNTs was significantly higher than that of HNTs [20]. Zhang et al. used a one-step hydrothermal method to coat the carbon layer on the surface of

* Corresponding author.
E-mail address: liumx@jnu.edu.cn (M. Liu).

https://doi.org/10.1016/j.msec.2019.110072
Received 11 January 2019; Received in revised form 10 August 2019; Accepted 10 August 2019
Available online 11 August 2019
0928-4931/

HNTs, which are more biocompatible in comparison of raw HNTs [21]. It can be precise to control of the reactant ratio in the hydrothermal reaction and easy to complete the synthesis as well as the crystallization of the products in one step, which performs better doping in the products [22]. The high thermal stability of HNTs suggests that HNTs are suitable to be functionalized by hydrothermal reactions.

Hydroxyapatite (HAP), similar to the mineral component of biological hard tissues of bones and teeth, shows fine osteoconductivity and bone bonding ability. Hence, HAP is used in biomedical field widely [23,24]. In general, HAP is served as one of the components of hard tissue replacement materials [25], including HAP-based ceramic composite [26], HAP-based bioactive glass composite [27] and HAP-polymer composite [28,29]. To improve biocompatibility and bioactivity of metal implants, HAP coating was introduced so that the advantages of metal alloys and HAP are combined [30]. Besides, HAP nanoparticles are capable of serving as vehicles for drug or protein to design drug delivery systems [31,32]. In bone tissue engineering, porous HAP ceramics are used as filling material for bone defects and drug release carriers [33]. In gene transfection studies, HAP has been extensively studied as a gene transfection vector [34,35]. HAP powder is prepared by two main ways, i.e. wet methods (precipitation, hydrothermal technique and hydrolysis of other calcium phosphates) and solid state reactions (sintering method) [25]. Among these methods, HAP prepared by hydrothermal reaction has a high degree of crystallinity and their crystal sizes range from nanometers to millimeters [36]. Especially, the plate-like HAP is suitable to apply for tissue engineering for the resemble morphology of inorganic phase of biological tissue [37,38]. The electrophoretic deposition method of chitosan composite films containing HNTs and HAP shows promising application in biomedical implants [39,40]. HAP particles are also prepared by in situ generation during sol-gel transition of suspension containing sodium alginate and HNTs, which can be employed in drug-controlled release matrices [41]. However, there is no report on anchoring HAP nanoparticles on HNTs by hydrothermal method.

In this study, rod-like hydroxyapatite@halloysite nanotubes (HAP@HNTs) are prepared by one-step hydrothermal method. HAP nanoparticles are bioactive to induce cells differentiation, while HNTs are used as mechanical enhancing material. The hybrid would combine the advantages of bioactive HAP and mechanical-strong HNTs. Additionally, the agglomerated behavior of HAP was partly solved by adding one-dimensional HNTs. The morphology and physical property of materials were investigated in detail. Using MC3T3-E1 preosteoblasts as a cell model, the biocompatibility and osteogenic differentiation properties of the materials were evaluated. In order to study the effect of HAP@HNTs as a functional enhancement phase to promote cell osteogenic differentiation, chitosan/HAP@HNTs composite films were prepared by solution casting method. This study includes the preparation and property of HAP@HNTs as well as the evaluation of its biocompatibility and osteogenic activity. HAP@HNTs can be used as functional filler for chitosan, which shows promising application as novel bone regeneration biomaterial as local delivery systems with improved osteoinductive properties.

2. Experimental

2.1. Materials

HNTs were purchased from Guangzhou Runwo Materials Technology Co., Ltd., China. HNTs were purified according to reference to remove the impurities [42]. Calcium nitrate ($Ca(NO_3)_2$) was supplied by Chengdu Aikeda Chemical Reagent Co., Ltd., China. Sodium phosphate (Na_3PO_4) was obtained from Tianjin Damao Chemical Reagent Co., Ltd., China. Ethanol was supplied by Tianjin Fuyu Fine Chemicals Co., Ltd. Chitosan (CS) was acquired from Jinan Haidebei Marine Bioengineering Co., Ltd., China. The deacetylation and viscosity-average molecular weight were 95% and 600,000 g/mol respectively. The other chemicals used directly in experiments were provided by Aladdin. Ultrapure water used in all experiments was from a Milli-Q water (resistivity > 18.2 MΩ·cm) system.

2.2. Synthesis of HAP@HNTs and CS/HAP@HNTs

HAP@HNTs were synthesized as follows [43]. HNTs were dispersed in 0.3 mol/L Na_3PO_4 solution. 0.5 mol/L $Ca(NO_3)_2$ solution was added drop by drop into the dispersion. Then, pH value was adjusted to above 10 using NaOH. The processes were completed under magnetic stirring at 60 °C. The volume of $Ca(NO_3)_2$ was same as that of Na_3PO_4 to ensure the calcium/phosphorus ratio is 5/3. The mixed dispersion was transferred to a Teflon-lined stainless-steel autoclave (50 mL), whose temperature was maintained at 180 °C for 16 h. After cooling down to room temperature, the white precipitate was washed by ethanol and centrifuged at low speed for 5 times. HAP@HNTs powder was obtained after drying and grinding. Four ratios between HAP and HNTs were set up to compare the structure and performance of HAP@HNTs, and the ratio of nanoparticles and HNTs is based on our previous study [21]. The product was denoted as HAP@HNTs with HAP and HNTs weight ratio. For example, HAP@HNTs 2-1 meant the weight ratio of HAP and HNTs was 2:1, which was abbreviated as 2-1.

The preparation of CS/HAP@HNTs composite film was illustrated in Fig. 1. Firstly, CS powder and HNTs or HAP@HNTs were added into ultrapure water under stirring. Glacial acetic acid, the amount of which was 1% of the dispersed solution, was added into the dispersion. Then, the dispersion became viscous. After being stirred for 12 h, the CS solution with powder was poured into a plastic petri dish and dry under 37 °C. The weight ratio of HNTs or HAP@HNTs was 5% relative to CS, because the composite films with 5% HNTs in previous study showed relatively good tensile properties and biocompatibility [2]. Residue acid in composite films was removed by soaking them in 0.1 mol/L NaOH for 2 h. The composite film was named CS/nanoparticles (such as CS/HNTs represented the composite film containing 5% HNTs). CS/HAP@HNTs referred to the 4 kinds of composite films, namely CS/1-2, CS/1-1, CS/2-1 and CS/4-1.

2.3. Characterization of HAP@HNTs

2.3.1. Transmission electron microscopy (TEM) and selected area electron diffraction (SAED)

The clay powder was mixed with ultrapure water by ultrasonication treatment to prepare 0.05 wt% suspension. The dispersion was dropped on a copper grid with carbon film supported. The samples were observed through TEM (JEM-2100F, JEOL Ltd., Japan).

2.3.2. Scanning electron microscopy (SEM)

The samples were prepared by drying the drops of diluted water dispersion of HAP@HNTs on glass sheet, which was analyzed by SEM (Ultra-55, Carl Zeiss Jena Ltd., Germany) at an accelerating voltage of 5 kV.

2.3.3. Dynamic light scattering (DLS)

The particles of HAP@HNTs were dispersed in ultrapure water with concentration of 0.05 wt%. The dispersion was ultrasonic for 30 min. The particle size was measured by a Nano-ZS instrument (Malvern Instruments Ltd., UK).

2.3.4. Brunauer–Emmett–Teller (BET) specific surface area and Barrett–Joyner–Halenda (BJH) pore analysis

To determine the specific surface area and pore size of raw or modified HNTs, the powder was verified by automated surface area and pore size analyzer (BeiShiDe 3H-2000, Instrument-ST. Co., Ltd., China). The adsorption and desorption curves were recorded.

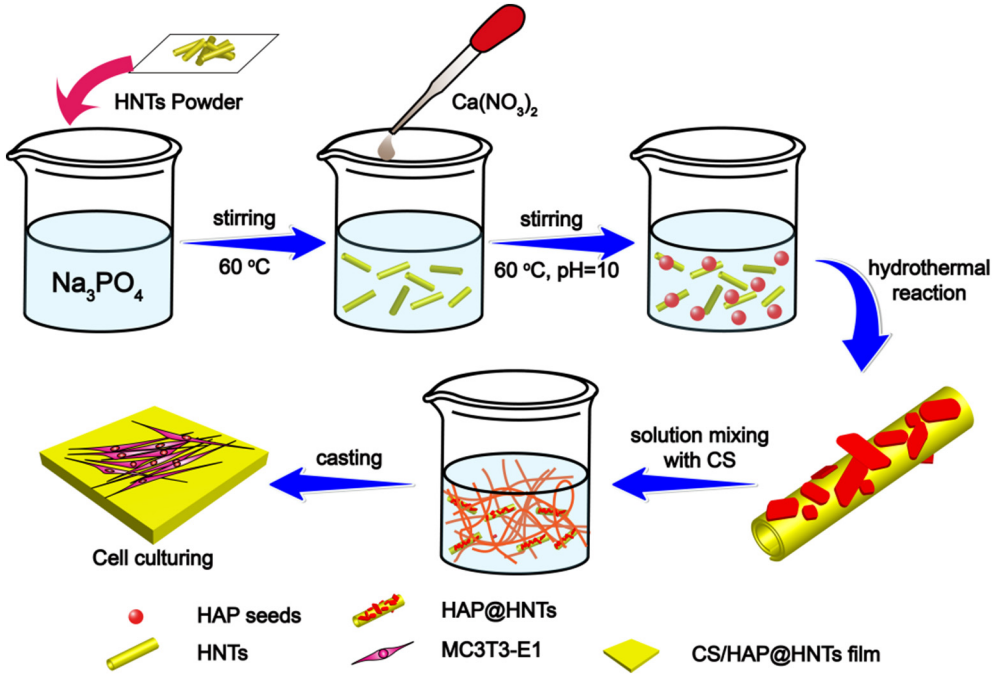

Fig. 1. Schematic illustration of the process of materials synthesis and cell culture.

2.3.5. Fourier transform infrared spectroscopy (FTIR)

The spectrum was recorded by a Thermo FTIR (Nicolet iS50, Thermo Fisher Scientific Ltd., USA) from 4000 cm^{-1} to 500 cm^{-1} to determine the surface functional groups of HAP@HNTs.

2.3.6. X-ray diffraction (XRD)

The XRD curves were tested by an X-ray diffractometer (MiniFlex-600, Rigaku Co., Japan) with scanning angle from 5° to 80° at scanning speed of 10°/min.

2.3.7. X-ray photoelectron spectroscopy (XPS) analysis

Atoms of Ca, P, Al, Si, and O of HAP, HNTs and HAP@HNTs 1-1 were detected by XPS instrument (ESCALAB250Xi, Thermo Fisher Scientific Ltd., USA).

2.3.8. Energy dispersive spectrometer (EDS) analysis

The samples of HAP@HNTs were analyzed at 200 kV by Field Emission Transmission Electron Microscope (JEOL 2100F, JEOL Ltd., Japan).

2.4. Characterization of CS/HAP@HNTs composite

The composite films were soaked in liquid nitrogen and the surface of brittle fracture was used to observe the dispersion of nanoparticles. The samples were observed by SEM (Ultra-55, Carl Zeiss Jena Ltd., Germany) at an accelerating voltage of 5 kV. The XRD curves of films were characterized by an X-ray diffractometer (MiniFlex-600, Rigaku Co., Japan) with scanning angle from 5° to 70° at scanning speed of 10°/min. The composite films were cut into rectangle shape with dimension of 5 × 1 cm. Tensile properties of samples at dry state and wet state were measured using a universal testing machine (UTM-Q422, Chengde Jinjian Testing Instrument Co., Ltd., China) at tensile rate of 2 mm/min. The XPS spectra were recorded by the XPS instrument (ESCALAB250Xi, Thermo Fisher Scientific Ltd., USA). Atoms of Ca, P, Si, and N were detected.

2.5. Cell culture

MC3T3-E1 preosteoblasts were purchased from the laboratory animal center of Sun Yat-Sen University, China. MC3T3-E1 cells were cultured in complete medium at 37 °C with atmosphere of 5% carbon dioxide (CO_2). The complete medium included minimum essential medium (MEM Alpha basic, Thermo Fisher Scientific Ltd., USA) supplemented with 10% fetal bovine serum (FBS, Thermo Fisher Scientific Ltd., USA) and 1% penicillin-streptomycin solution (Jiangsu KeyGEN BioTECH Ltd., China). When the cells grew to 80% confluences in cell culture flask, cell passage was performed. Then, the cells were washed by phosphate balanced saline (PBS, Thermo Fisher Scientific Ltd., USA) and treated with trypsin/ethylenediaminetetraacetic acid (Jiangsu KeyGEN BioTECH Ltd., China) for 1 min to get the cell suspension. The cell suspension was centrifuged and the upper liquid was poured out. The cell suspension was re-obtained by adding complete medium, followed by cell culture.

2.6. Cell counting kit-8 (CCK-8) assays

2.6.1. HAP@HNTs

MC3T3-E1 cells were seeded in 96-well plates with cell seeding density 8 × 10^3 cells/well and cultured at 37 °C for 24 h. Then, complete culture medium with HNTs, 1-2, 1-1, 2-1, and 4-1 at different concentrations (0, 10, 25, 50 and 100 μg/mL) was added into the wells. The cells were washed with PBS twice after culture and 100 μL CCK-8 reagents (Shanghai BestBio Technology Co., Ltd., China) was added into each well. The cells with CCK-8 reagents were placed in the incubator for 4 h. In order to reduce the influence of materials on result, the tested liquid was centrifuged at 15,000 rpm and the absorbance of the supernatant at 450 nm was measured through a microplate reader. Cell viability was the absorbance ratio of the sample to that of the control group.

2.6.2. CS/HAP@HNTs

MC3T3-E1 cells (5 × 10^3 cells/well) were seeded on composite film in 96-well plates and cultured at 37 °C. On day 1, day 3 and day 5, the tested cells were washed by PBS. 100 μL the mixture of new medium and CCK-8 reagents were added to incubate for 4 h. Afterwards, the mixture in each well was moved to measure the optical density (OD) values at 450 nm through a microplate reader.

2.7. Acridine orange/ethidium bromide (AO/EB) staining assays

2.7.1. HAP@HNTs

MC3T3-E1 cells were seeded in 96-well plates (8×10^3 cells/well) and cultured for 24 h. Then, the cells were cultured for 24 h with complete culture medium containing HNTs, 1-2, 1-1, 2-1 and 4-1 at different concentrations (0, 10, and 50 μg/mL). Cells were stained by AO/EB staining kit (Beijing Solarbio Technology Co., Ltd., China) and observed using a fluorescence microscope (XDY-2, Guangzhou Liss Optical Instrument Ltd., China).

2.7.2. CS/HAP@HNTs

MC3T3-E1 cells (5×10^3 cells/well) were transferred on composite film in 96-well plates and cultured at 37 °C for 1, 3, 5 days. Then, cells were stained by 10 μL mixtures of AO (100 μg/mL) and EB (100 μg/mL), and observed through a fluorescence microscope.

2.8. Alkaline phosphate (ALP) activity assays

The cells cultured for 7 days and 14 days were washed by PBS twice. To investigate osteogenic differentiation, the supernatant of cells lysis with RIPA tissue/cell lysate (Beijing Solarbio Technology Co., Ltd., China) was taken for activity detection. ALP activity was determined by alkaline phosphatase assay kit (Shanghai BestBio Technology Co., Ltd., China) and bicinchoninic acid (BCA) protein quantitative kit (Shanghai BestBio Technology Co., Ltd., China). Besides, the cells were fixed by 4% paraformaldehyde for 10 min and stained for 20 min by alkaline phosphatase staining solution which was based on azo coupling method (Beijing Leagene Biotech Co., Ltd., China). The images were taken using an optical microscope.

2.9. Alizarin red S (ARS) staining and calcium deposition assays

The cells were cultured for 21 days and then fixed by 4% paraformaldehyde after washing by PBS. The calcium deposition was stained using 1% alizarin red (Beijing Leagene Biotech Co., Ltd., China) for 30 min. The samples were washed by ultrapure water and observed under a microscope. 100 mM 1-dodecylpyridinium chloride was utilized to ascertain the amount of calcium deposition semi-quantitatively. The results were shown by the absorbance at 562 nm.

2.10. Quantitative real-time polymerase chain reaction (qRT-PCR)

The cells were harvested by trizol (Thermo Fisher Scientific Ltd., USA) at a certain time. After being extracted, the RNA was inactivated using RNase-free DNase (R) (Beijing Promega Biotechnology Co., Ltd., China) and de-genomic. After detecting the purity and integrity of the mRNA, it was reversely transcribed into complementary DNA (cDNA) (the reagents used were all from Promega). qRT-PCR was performed by an ABI PRISM® 7500 Sequence Detection System. The primer sequences are given in Table 1. The relative quantification of mRNA (ALP, COL I, RUNX2, OCN) was determined by $2^{-\Delta\Delta Ct}$ method while β-action was used as a housekeeping gene.

Table 1
RT-PCR primer sequences.

Gene	Primer sequences
ALP-F	5′ CGCTATCTGCCTTGCCTGTA
ALP-R	5′ GGTTGCAGGGTCTGGAGAAT
COL I-F	5′ CTTCACCTACAGCACCCTTGT
COL I-R	5′ AAGGGAGCCACATCGATGAT
RUNX2-F	5′ TGCCCAGTGAGTAACAGAAAGAC
RUNX2-R	5′ CTCCTCCCTTCTCAACCTCTAA
OCN-F	5′ AGGGCAATAAGGTAGTGAA
OCN-R	5′ CGTAGATGCGTCTGTAGGC
β-actin-F	5′ GCTTCTAGGCGGACTGTTAC
β-actin-R	5′ CCATGCCAATGTTGTCTCTT

2.11. Statistical analysis

The data were presented as means ± standard deviation (SD). Statistical comparisons of data were performed using SPSS Statistics 22.0 for one-way analysis of variance (ANOVA). The significant levels were with (*) for $P < 0.05$ and (**) for $P < 0.01$.

3. Results and discussions

3.1. Characterization of HAP@HNTs

The synthesis method of HAP by hydrothermal process was performed according to the reference [43]. The Ca/P ratio of reagent was controlled at 5/3 with a pH of 10. Pure HAP particles are < 50 nm in length and 20 nm in width as shown in Fig. 2A. For the synthesis of HAP@HNTs, HNTs were dispersed in Na_3PO_4 solution adequately before adding $Ca(NO_3)_3$. HAP seeds are around outside of HNTs without other treatments of their lumen. After hydrothermal reaction, HAP was generated evenly on the surface of the tubes. As the proportion of HNTs decreases, the number of HAP nanoparticles adhered to the surface of the tubes increases, as shown in the SEM images of Fig. 2A. It also has been reported that there is clear existence of van der Waals force between nanoparticles and nanotubes [44–46]. Similarly, the morphology of HNTs is typical nanotube and the size of prepared HAP particles is in nanoscale. Thus, there should be van der Waals force between HNTs and HAP, and their detailed interactions will be studied in following work. The interplanar spacing of 0.790 nm is observed from the HR-TEM image in Fig. 2B, which is influenced by HNTs to cause measurement error and may correspond to (100) plane of the hexagonal HAP [,47]. There are discontinuous diffraction spots on the SAED image, indicating that the crystals of synthesized HAP are single crystals with random orientation [48]. In the detection region, the planes with strong reflections correspond to (002) plane and (211) plane, respectively, and the corresponding interplanar spacing is 0.34 nm and 0.28 nm. Since the synthesized HAP grains are on the surfaces of HNTs, the diffraction patterns are interfered by HNTs. Fig. 2C illustrates the particle size of different nanomaterials in water. The particle size distribution of a small portion of HAP ranges in 550–700 nm. The smaller the size of nanoparticles is, the greater the surface energy is. As a result, the agglomeration of HAP may occur on the surface of HNTs [49]. The particle size distribution of HAP mainly ranges from 4 to 6 μm, while pure HNTs exhibit good nanoscale dispersion in water. The particle size of HNTs exhibits two peaks around 180 nm and 600 nm. The particle size distribution of the HAP@HNTs 1-1 is from 100 to 300 nm and 600 to 1100 nm. This range is covered with the size distribution range of HNTs. It suggests that HAP is mainly distributed on the outer surfaces of the tubes. Therefore, the aggregation of HAP nanoparticles is significantly reduced by the incorporation of HNTs.

The N_2 adsorption performance of different nanoparticles is determined by specific surface area. The BET specific surface area of HAP, HNTs, and HAP@HNTs (1-2, 1-1, 2-1, 4-1) are 51.8, 57.4, 62.1, 53.2, 52.4, 50.8 m^2/g, respectively. The maximum desorption value of HAP, HNTs and HAP@HNTs (1-2, 1-1, 2-1, 4-1) are 274.2, 217.6, 262.7, 232.2, 225.6, 218.7 mL/g, respectively (Fig. 3A). The adsorption ability of HAP is high since they have large specific surface area. The adsorption capacity of HAP@HNTs decreases with the increasing ratio of HAP as well as the decreased specific surface area. When a small amount of HAP is distributed among the clay tubes, the specific surface area and adsorption performance are greater than that of pure HNTs. This is due to the incorporation of nanoparticles with much lower size. However, when a large number of HAP particles are introduced outside the tubes, part of the pores on HNTs are blocked and part of HAP nanoparticles aggregate. Consequently, the specific surface area and

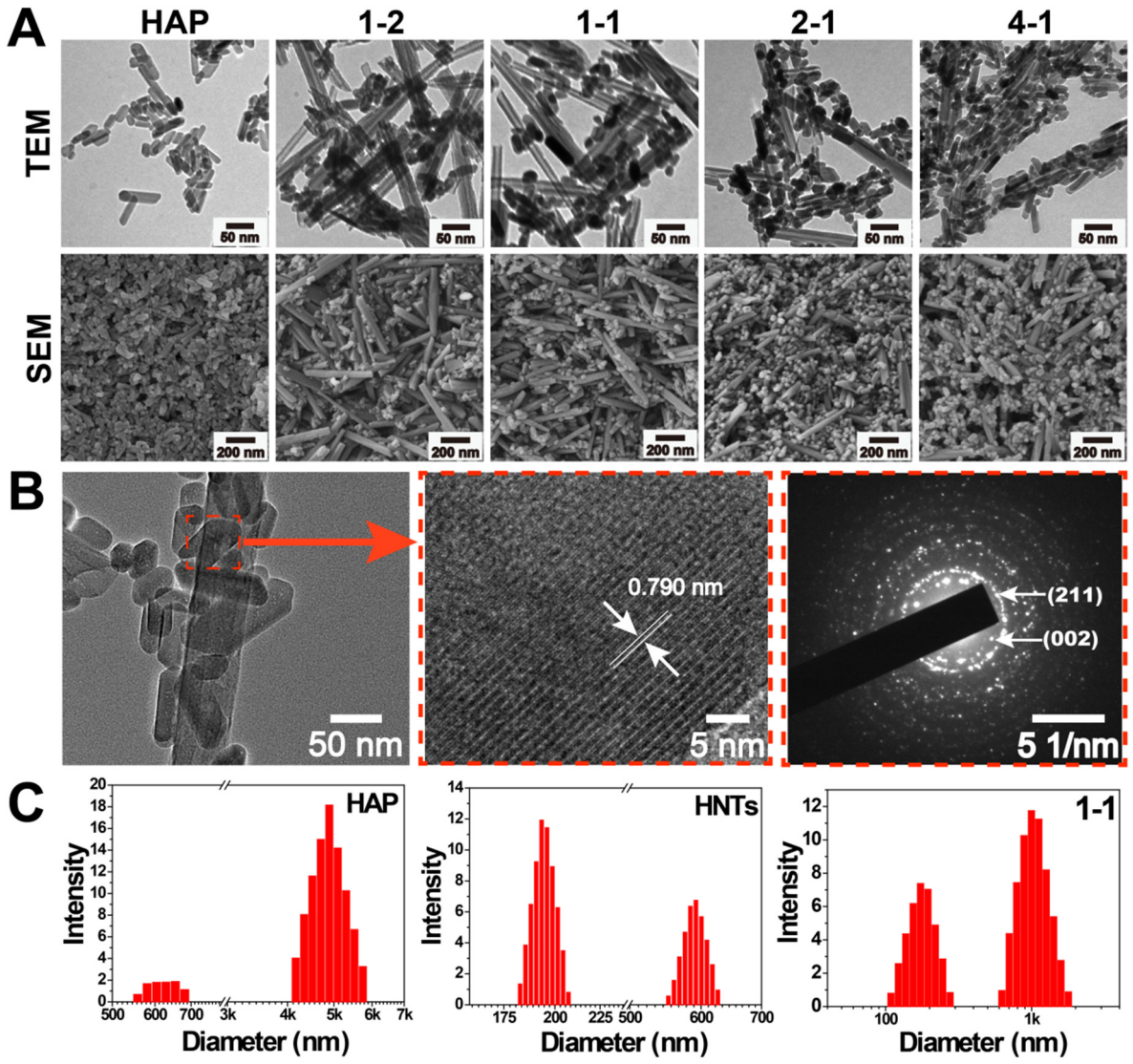

Fig. 2. TEM and SEM images (A) of HAP and HAP@HNTs (1-2, 1-1, 2-1, 4-1); HR-TEM and SAED images (B) of HAP@HNTs 2-1; DLS results (C) of HAP, HNTs and HAP@HNTs 1-1.

adsorption performance of the hybrid are reduced. As shown in Fig. 3B, the pore volume gradually decrease with the increase in the amount of HAP, although the peaks of HAP@HNTs are similar to that of HNTs [50]. Unlike the amorphous carbon layer outside HNTs, HAP nanoparticles have little effect on the pores on HNTs [21]. The carbon layer can wrap the tubes completely and cover the pores of HNTs, while HAP is only anchored on the tubes' surface. All the samples show pore distribution from 2 to 100 nm. The results indicate that HAP@HNTs are prepared successfully, and HAP does not completely cover the surface of HNTs.

Fig. 3C shows FTIR spectrum of HAP, HNTs and HAP@HNTs 1-1. The peaks of 3695 cm^{-1} and 3625 cm^{-1} are assigned to the stretching vibration peaks of external hydroxyl and inner hydroxyl bands. The peaks at 1016 cm^{-1} and 908 cm^{-1} belong to deformation vibration of Si—O and O—H bonds at internal hydroxyl [51]. The FTIR spectrum of HAP@HNTs 1-1 contains the infrared absorption peaks of HAP. The peaks of 1091 cm^{-1} and 1036 cm^{-1} are due to the P—O asymmetric stretching of $(PO_4)^{3-}$. The peaks of 602 cm^{-1} and 564 cm^{-1} are the results of P-O-P bending vibration. These indicate that HAP is successfully synthesized and evenly distributed outside HNTs [52]. The crystal characteristics of the HAP@HNTs are further demonstrated by XRD patterns (Fig. 3D). The main diffraction peaks of HAP appear at 25.8°, 28.2°, 29.1°, 31.9°, 32.3°, 33.1°, 34.2°, whose corresponding planes are (002), (102), (210), (211), (112), (300), (202) [53]. For the XRD diffraction patterns of HAP@HNTs, the diffraction peaks of HAP are included. The corresponding peak strength is different which arise from the different ratio of HNTs and HAP. With the increase of the HAP ratio, the XRD pattern of HAP@HNTs is more similar with that of HAP. There are three peaks at 11.8°, 20.1°, 25.1° in the curves belonging to (001), (020, 110) and (002) planes of HNTs [54]. The present XRD pattern of HAP@HNTs is similar to the XRD result of reference [39]. All they show that the diffraction peaks of HAP have covered the peaks of HNTs with increasing the ratio of HAP. So, the peak strength of HNTs decreased significantly in the XRD curves of HAP@HNTs.

To analyze the elements on the surface of the material, the material was characterized by EDS (Fig. S1). There are 5 kinds of elements in 1-1 powder, i.e. Ca, P, Si, O, Al. The elements of Ca and P are from HAP mainly, while Al and Si are brought by HNTs. The measured element content (Ca and Si) is partly interfered by the glass slide as a substrate for the determination. Therefore, the ratio of Ca to P is < 1.67 and a peak of Si appears in the EDS spectrum of pure HAP. In order to further study the surface elements of HAP@HNTs 1-1, the material was characterized by XPS, as shown in Fig. 4A. The XPS spectrum of detected HAP powder is dominated by three elements: O (53.5%), Ca (17.51%)

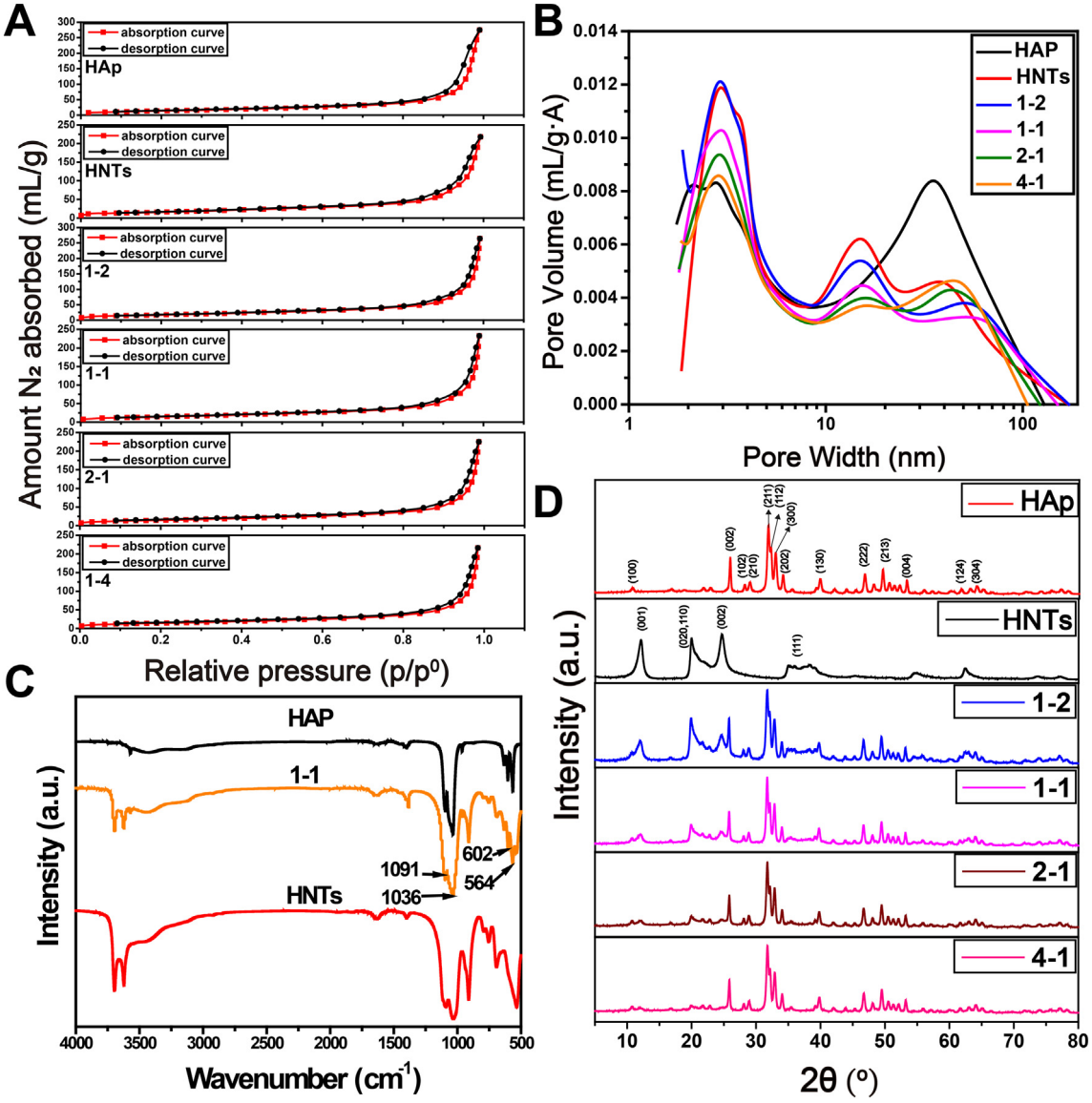

Fig. 3. N_2 adsorption-desorption curves (A), BJH pore analysis (B), FTIR spectrum (C) and XRD pattern (D) of HAP, HNTs, and HAP@HNTs.

and P (12.49%), while HNTs mainly contain Al (14.46%), Si (15.88%) and O (61.79%). A small amount of C may come from the residual carbides in the hydrothermal reactor and the dust in the laboratory equipment. In comparison of HAP, Al in HAP@HNTs 1-1 powder increases from 0.18% to 9.13%, while Si and O change severally from 0.26% to 9.98% and 53.5% to 61.03%, respectively. The atomic percentages of Ca and P slightly decrease. These suggest the hybrid has both components of HAP and HNTs. The binding energy of corresponding elements (Ca, P and O) on HAP@HNTs 1-1 moves towards the high binding energy, relative to pure HAP (Fig. 4B). The binding energy of Ca2p of HAP is 347.2 eV and 350.8 eV, while that of HAP@HNTs 1–1 is 347.5 eV and 351.0 eV. The binding energy of P2p is also slightly shifted by 0.1 eV in comparison to that of HAP, while the binding energy of O2p changes from 532.2 eV to 531.3 eV. As for Si and Al elements, their binding energies in HAP@HNTs 1-1 are lower than those of raw HNTs. The change in binding energy is caused by the addition of HNTs during the synthesis of HAP. The chemical environment of the atoms of HAP and HNTs is affected via van der Waals force and hydrogen bonding interactions [55].

3.2. Evaluation of cytocompatibility of HAP@HNTs in vitro

To study the toxicity of the material to cells, MC3T3-E1 cells were cultured by the complete culture medium with a certain amount of material and the activity of the cells was determined. Fig. 5A shows the relative cell viability of MC3T3-E1 cells which are treated with HNTs and HAP@HNTs at different concentrations for 24 h. For the same material, as the concentration of the material increases, the cell activity decreases. This phenomenon is explained by the fact that both HNTs and HAP@HNTs are inorganic substances which tend to deposit in the bottom of the solution and affect the growth of the cells. At the same concentration, the cytocompatibility ofHAP@HNTs is significantly better than that of pure HNTs on account of the good biocompatibility of HAP. There are significant differences between HAP@HNT groups and HNT groups ($P < 0.05$ or $P < 0.01$). When the added amount of HAP@HNTs is < 50 μg/mL, the cell activity after 24 h of incubation with the material is > 90%. Fig. 5B displays the images of staining cells under a fluorescence microscope. The green part is the nucleus of living cells stained by AO reagent, and the red part is the nucleus of dead cells stained by EB reagent. The staining results of AO/EB are consistent with the results of the CCK-8 experiment. Dead cells in the HNT group are

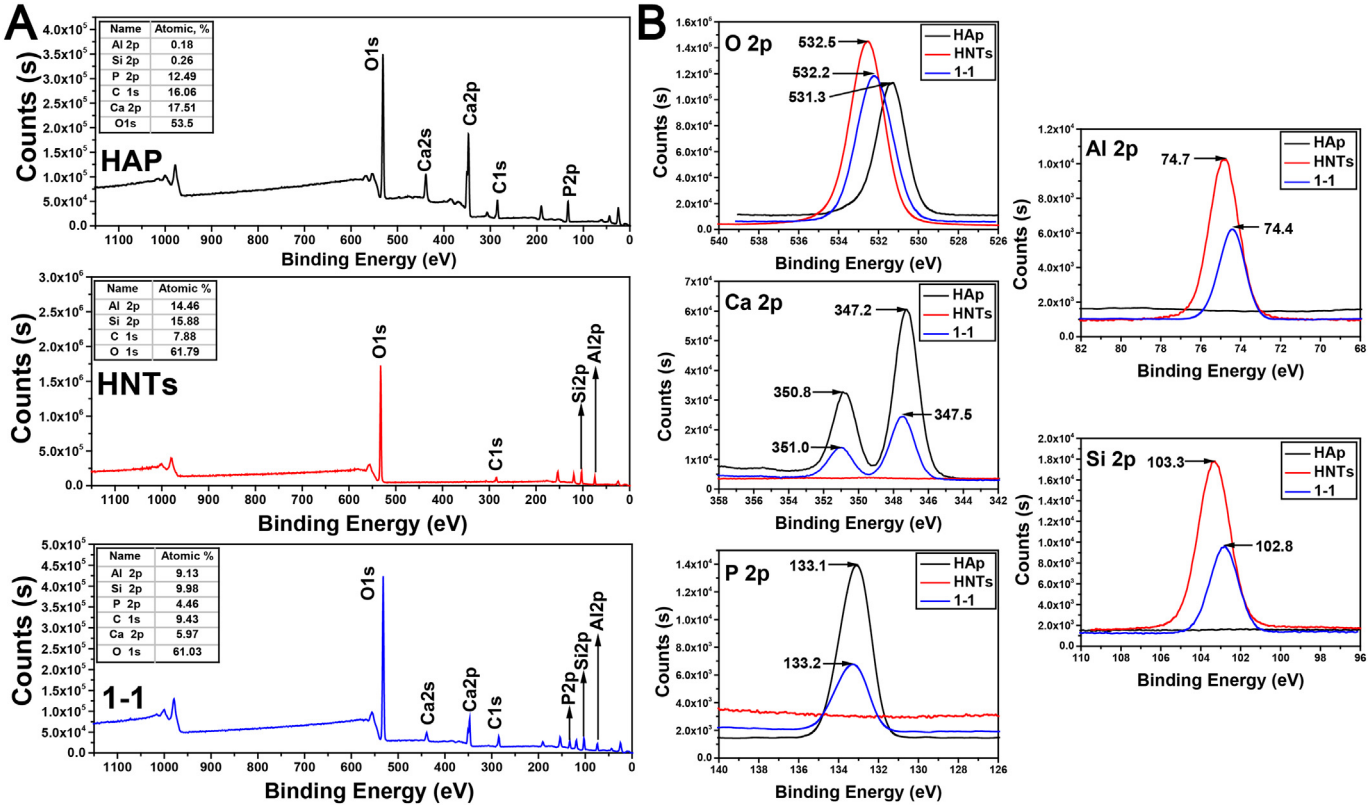

Fig. 4. The survey of XPS spectra (A) of HAP, HNTs and HAP@HNTs 1-1, high-resolution scanning (B) of corresponding element (O, Ca, P, Al and Si).

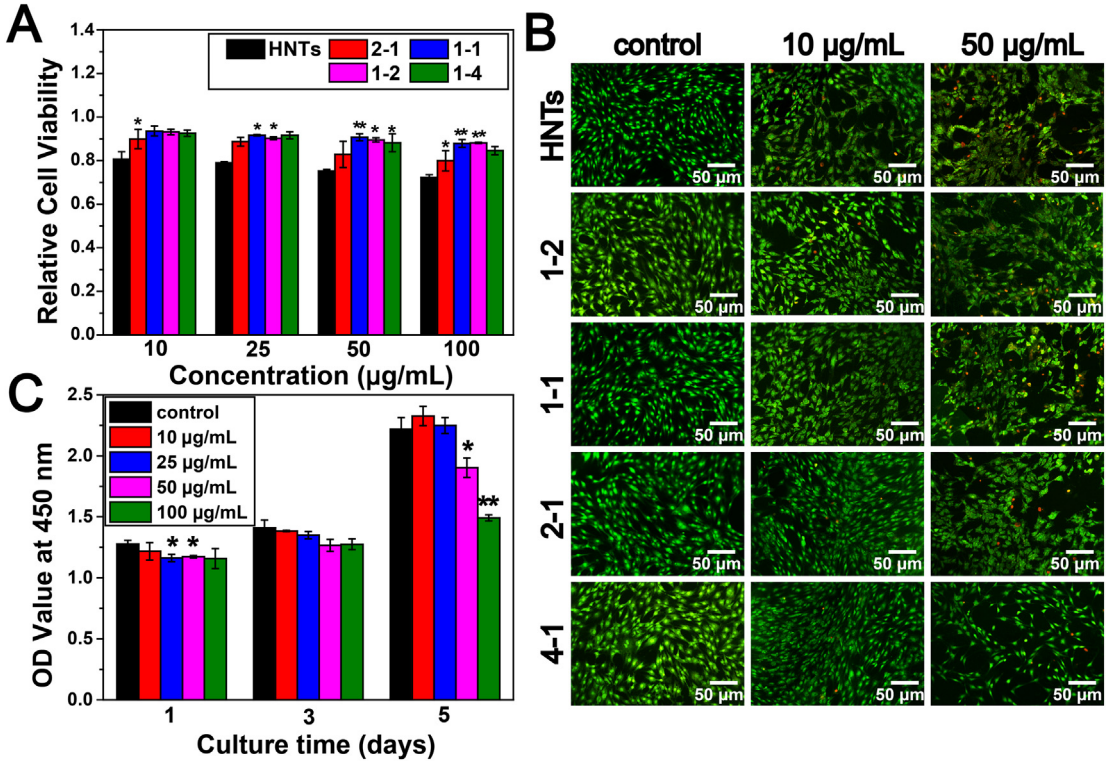

Fig. 5. The relative viability (A) of MC3T3-E1 cells cultured with HNTs and HAP@HNTs at different concentration after 24 h; The photos (B) of AO/EB staining of MC3T3-E1 cells treated with HNTs and HAP@HNTs at the concentration of 0, 10, 50 μg/mL for 24 h; The OD value (C) of MC3T3-E1 cells being treated with 2-1 after 1, 3 and 5 days. The results are presented as mean ± SD ($n = 24$) in 3 separate experiments. The data were analyzed by SPSS Statistic 22.0. *$P < 0.05$; **$P < 0.01$ versus HNT or control group.

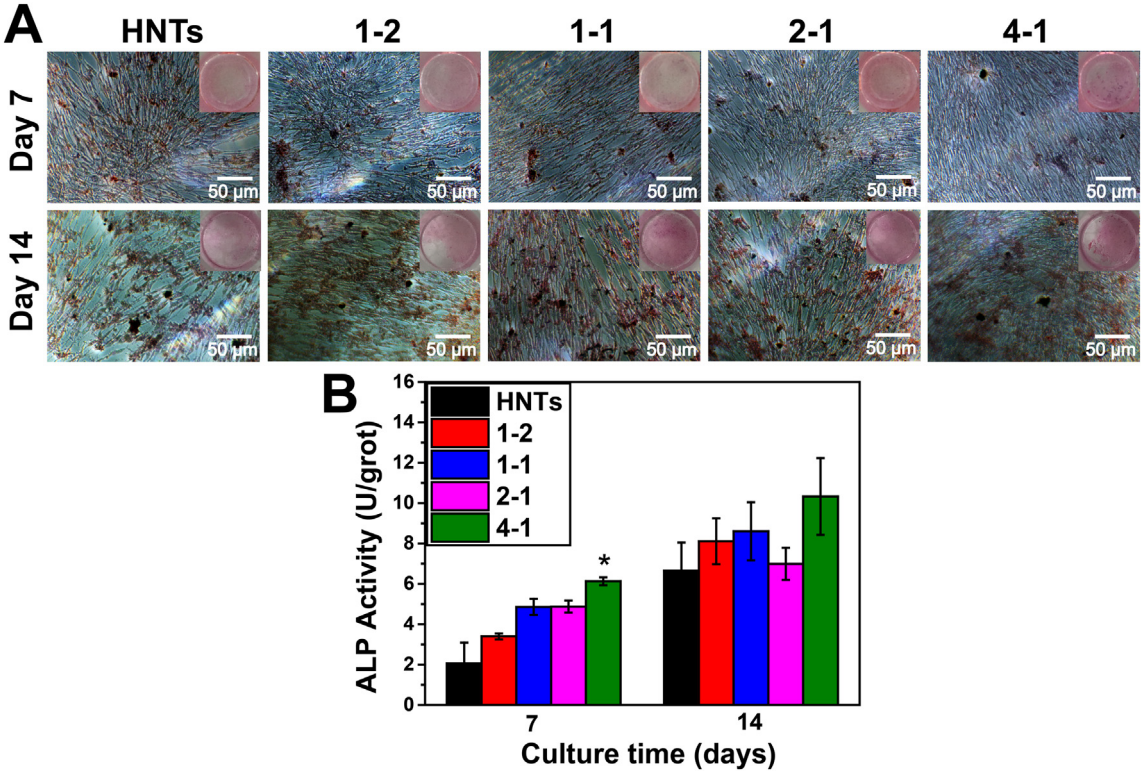

Fig. 6. The photos of ALP staining (A) and ALP activity (B) of MC3T3-E1 cells cultured with HNTs and HAP@HNTs at 25 μg/mL after 7 days and 14 days. The results are presented as mean ± SD (n = 24) in 3 separate experiments. The data were analyzed by SPSS Statistic 22.0. *P < 0.05 versus HNTs group.

more than that of HAP@HNT group under additional amount at 50 μg/mL, while HAP@HNT groups show slower cell proliferation. The cells are less affected when they are treated with 10 μg/mL nanoparticles. Moreover, HAP@HNTs 1-2 is selected to study the effect of incubation time and material addition on MC3T3-E1. In comparison with the blank groups, the activity of the cells is high when the addition amount is < 25 μg/mL (Fig. 5C). Above 50 μg/mL, the OD values decrease obviously, especially on day 5 (P < 0.05). All these results suggest the improved cytocompatibility of HNTs by anchoring HAP. There has been widely used of calcium phosphate bioceramics for bone regeneration applications, such as HAP and tricalcium phosphate. Their biocompatibilities are thought to be due to their chemical and structural similarity to the mineral phase of native bone. HAP is known to enhance osteoblast differentiation as well as osteoblast growth. [56] Therefore, we attach HAP on HNTs for improving the cytocompatibility especially the osteoblast differentiation of HNTs.

HAP is considered with ability to promote the differentiation of preosteoblasts. Therefore, the effect of HAP@HNTs on the osteogenic differentiation of MC3T3-E1 cells is then investigated. The early osteogenic differentiation level of osteoblasts is reflected by the activity level of ALP which is a specific protease secreted by cells. From the images of ALP staining (Fig. 6A), the cell morphology becomes slender because of their differentiation. The ALP present in the cells is blue-gray, while the ALP secreted by the cells is stained to be positive particles. On day 7, cells cultured with HAP@HNT groups express ALP activity higher than that of cells cultured with HNTs. Additionally, the higher the proportion of HAP is, the more obvious the blue-gray part is in the cytoplasm of the stained cells and the more positive particles are outsides the cells. The cell density cultured for 14 days with HNTs is less than that of 7 days, but this difference is smaller in HAP@HNT groups. Pure HNTs have a negative impact on the long-term growth of cells. This effect is reduced by anchoring HAP outside the tubes. However, the ALP activity of the cells at day 14 is higher than that of the cells at day 7 in each group, which can be found out from the number and size of positive particles. From Fig. 6B, it is also can be seen that the ALP activity of the cells cultured for 14 days is significantly higher than that of 7 days for each group. The ALP activity increases from 2.05, 3.39, 4.86, 4.88, 6.13 U/grot to 6.65, 8.11, 8.61, 6.98, 10.33 U/grot for each group respectively, which are consistent with the results of ALP staining. These results indicate that HAP@HNTs with excellent cytocompatibility are able to promote osteogenic differentiation of cells. The pictures in the upper right corner of Fig. 6A are digital photos of each group after dyeing. From these results, the biocompatibility and the osteogenic property of HAP@HNTs are improved in comparison of raw HNTs because HAP@HNTs contain HAP which is well known for its special biological property. It can be concluded that the good biocompatibility of HAP@HNTs is mainly due to the features of HAP.

3.3. Characterization of CS/HAP@HNT composite film

HAP@HNTs was added to chitosan to prepare composite film and the film properties were further explored. Fig. 7A shows the SEM images of the cross section of composite film. The cross section of CS film is smooth with some microcracks occurred during the drying of the film. In picture b of Fig. 7A, HNTs appear as uniformly distributed white spots, which are homogenously dispersed in CS matrix. Pictures (picture c to picture f) in Fig. 7A are the cross sections of HAP@HNTs (1-2, 1-1, 2-1, 4-1) that are mixed with CS. The size of the particles in the section reflects the dispersion performances of HAP@HNTs in aqueous solution. HAP tends to agglomerate into larger particles in solution, so the more HAP is added, the more obvious this phenomenon is. It is confirmed by the large particles that aggregate in CS/4-1 composite film. Fig. 7B displays XRD patterns of CS film and the composite films. The diffraction peaks of CS film nearby 10.2° and 20.1° are attributed to (020) and (110) planes [51]. In the diffraction pattern of CS/HNTs, the diffraction peak at 12° belongs to (001) plane of HNTs. The large peak between 18° and 25° is the result of the overlap of (020, 110), (002) planes of HNTs and (110) plane of chitosan. The peaks of

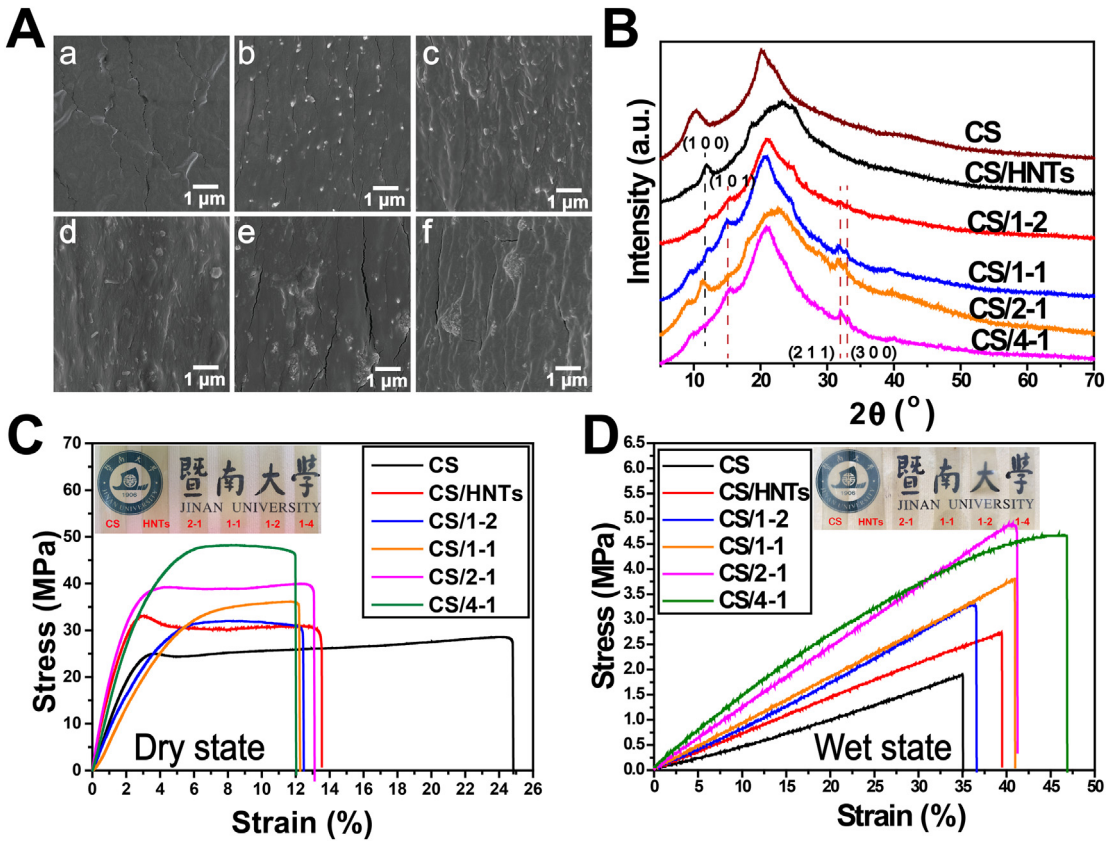

Fig. 7. SEM images (a to f: CS, CS/HNTs, CS/1-2, CS/1-1, CS/2-1, CS/4-1) (A), XRD pattern (B), stress and strain curves at dry state (C) and wet state (D) of the composite films.

Table 2
Tensile mechanical properties of composite films.

Samples	Dry state		Wet state	
	Tensile strength (MPa)	Elastic modulus (MPa)	Tensile strength (MPa)	Elastic modulus (MPa)
CS	28.61 (2.05)	856.1 (31.2)	1.87 (0.15)	4.4 (0.3)
CS/HNTs	30.80 (2.23)	879.8 (28.5)	2.71 (0.19)	7.1 (0.1)
CS/1-2	32.32 (2.68)	881.6 (37.6)	3.27 (0.21)	8.2 (0.2)
CS/1-1	36.35 (3.06)	738.5 (40.9)	3.80 (0.22)	9.1 (0.3)
CS/2-1	40.22 (2.87)	1542.3 (52.3)	4.87 (0.24)	12.1 (0.4)
CS/4-1	48.31 (3.61)	1427.4 (47.7)	4.71 (0.21)	13.4 (0.3)

CS/HAP@HNT composite film at 15.3°, 31.8°, 33.0° are caused by HAP, which correspond to (101), (211), (300) planes of HAP. Fig. 7C (at dry state) and Fig. 7D (at wet state) are the stress-strain curves to show the tensile mechanical properties of films. Table 2 summaries the tensile mechanical property data of films. It can be seen that the tensile strength and elastic modulus are enhanced by the incorporation of HNTs or HAP@HNTs simultaneously. For example, the tensile strength and elastic modulus of CS/4-1 are 48.31 MPa and 1427.4 MPa at dry state, while the pure CS film only display 28.61 MPa in tensile strength and 856.1 MPa in elastic modulus. As natural one-dimensional nanomaterial, HNTs and HAP@HNTs exhibit high reinforcing ability towards CS. There are interfacial interactions between HNTs and CS such as hydrogen bonding and electrostatic attraction [2,57]. The strong interfacial interaction between CS and powder materials promotes the tensile strength and the elastic modulus of composite films.

In order to investigate chemical composition of the different film, XPS was used to characterize the elements (Fig. S2). There are 3 main elements on the surface of CS film, namely C, O and N. The main detected elements are Ca, P, Si and N in this test, while O and C are not included. The characteristic elements of HNTs and HAP appear in the CS/1-1 survey for HAP@HNTs 1-1. The atomic percentages of Al and Si rise from 3.75% and 1.15% to 12.66% and 8.54%, respectively, while the ratio of Ca and P is increased from 4.3% and 5.73% to 22.01% and 17.17%, respectively. The XPS result indicates that some HAP@HNTs is distributed on the surface of films.

3.4. Evaluation of cytocompatibility of CS/HAP@HNT composite film

HAP@HNTs have good biocompatibility to promote osteogenic differentiation of cells from the result above. HAP@HNTs are partially exposed on the composite film surfaces, so the cytocompatibility of the composite films is supposed to be improved. The toxicity test results of composite films are shown in Fig. 8. Fig. 8A displays the images of AO/EB staining of MC3T3-E1 cells cultured for 1, 3, 5 days. The green fluorescent spots are the stained living cells and the red fluorescent spots are the stained dead cells. The images show the number of cells and the morphology of the cells adhering to various film. Because of relatively small content of nanoparticles to CS, there is no difference in cell morphology between the CS film and the composite film. The cells on the first day show that the cell activities of the film are approximately same. On day 3, the number of dead cells on CS/2-1 and CS/4-1 is lower than that of other groups. In comparison with the result on day 1, the cell density of each group on day 3 increased markedly and the cell morphology is similar, which demonstrates that the cells are mainly divided during this period. The cell density on each film on day 5 further increases, and the morphology of the cells becomes slender which may indicates that the cells have transitions from cell division to cell differentiation. A small amount of EB dye is difficult to clean on the cell membrane. It causes red fluorescence on the cytoplasm of the cells such as the picture of CS on day 3. Fig. 8B shows the result of CCK-8

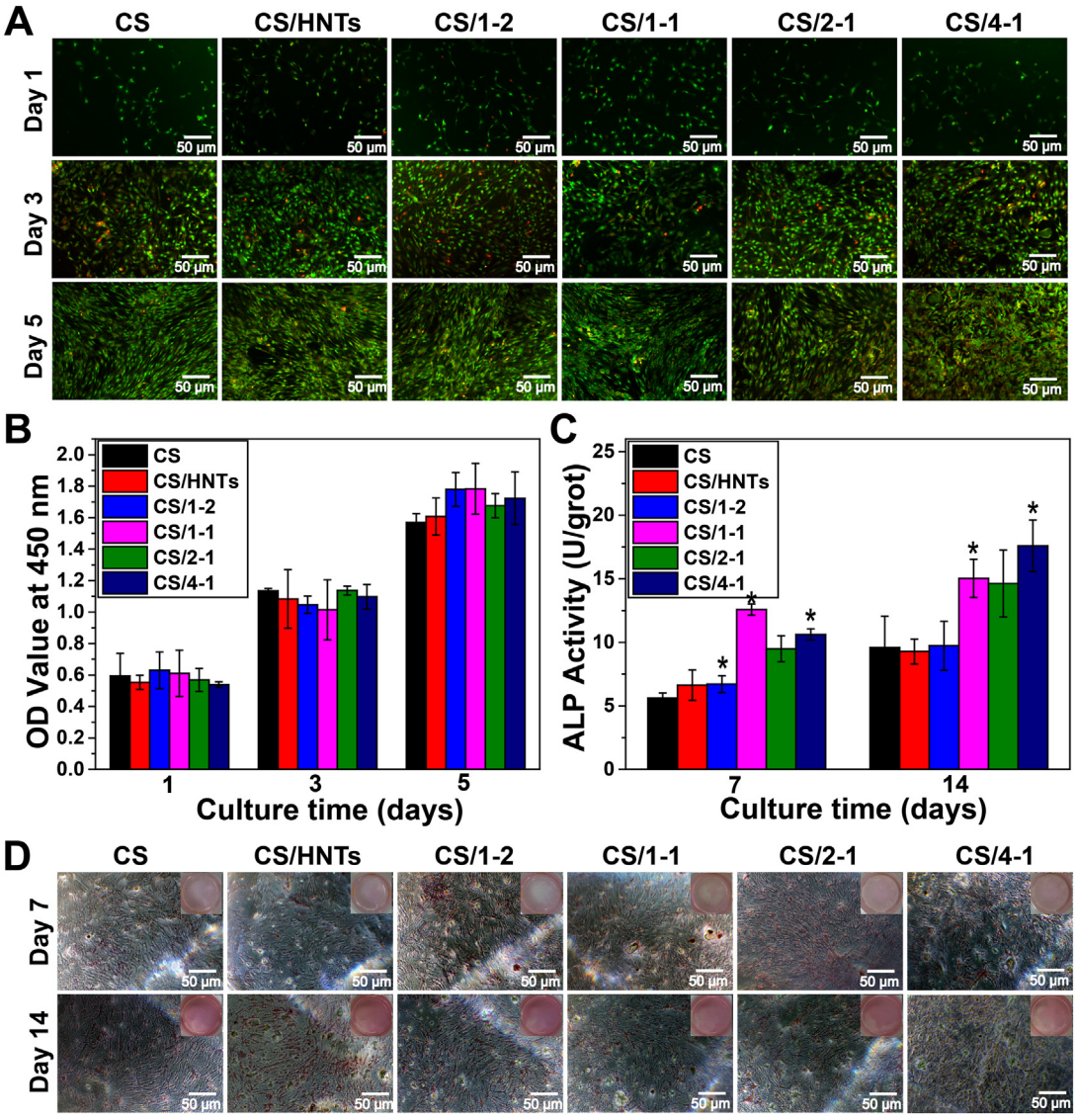

Fig. 8. The photos of AO/EB staining (A) and the OD value (B) of MC3T3-E1 cells culturing on films after 1, 3, 5 days; The ALP activity (C) and the images of ALP staining (D) of MC3T3-E1 cells cultured on the composite films after 7 and 14 days. The results are presented as mean ± SD ($n = 24$) in 3 separate experiments. The data were analyzed by SPSS Statistic 22.0. *$P < 0.05$ versus CS group.

assay of MC3T3-E1 cells seeded on film for 1, 3, 5 days. The results are determined by the OD values at 450 nm and are consistent with Fig. 8A. As the culture time increases, the activity of the cells increases. On the day 5, the cell activity on the CS/HAP@HNT films is better than that on the CS film and the CS/HNT film.

The cell culture time is prolonged to study the ability of the composite film about promoting osteogenic differentiation of the MC3T3-E1 cells. Fig. 8C shows ALP activity of MC3T3-E1 cells cultured on the composite film after 7 and 14 days. The ALP activity of cells on the composite film is higher than that on the CS film and the CS/HNTs film, especially CS/1-1, CS/2-1 and CS/4-1 (in comparison with CS group, $P < 0.05$). HAP@HNTs 1-1 particles are more easily dispersed in the film than 2-1 and 4-1, while there is enough HAP to wrap HNTs in comparison to 1-2. On day 7, the ALP activity of cells on CS/1-1 is highest among the groups. It suggests that the degree of cell differentiation is greatest. However, it results in a small increase (2.46 U/grot) in ALP activity on day 14. The ALP activity of CS/2-1 and CS/4-1 increases 5.13 U/grot and 6.98 U/grot respectively. The evidence is also provided by Fig. 8D. The long and thin parts with blue-gray are the stained cells. The cells at 14 days are darker and have more blue-gray particles around them. The cell density at both time points is consistent. The pictures in the upper right corner of Fig. 8D are digital photos of each group after dyeing.

With the cell differentiation, calcium phosphate is deposited and then mineralized into calcium nodules, especially in the late stage of osteogenic differentiation. ARS is an anthraquinone compound that can be complexed with Ca^{2+} to form a red or orange-red complex. After 21 days of cell culture, the cells are stained with 1% ARS to indirectly characterize the number of calcium nodules. The 1-dodecylpyridine chloride solution could extract the complex. The amount of extraction is determined as the absorbance at 562 nm. As shown in Fig. 9A, the deposited calcium nodules on CS film are scattered around the cells with deep red dots, and the result on CS/HNTs is similar. It is evident that the quantity of calcium nodules deposited on CS/HAP@HNTs increases. Even in some areas, they are distributed in a sheet as CS/2-1 and CS/4-1. Fig. 9B displays the semiquantitative result of the absorbance. The MC3T3-E1 cells on the HAP-containing film have a large number of mineralized calcium nodules in contrast to the cells on CS ($P < 0.05$ or $P < 0.01$). The content of HAP is positively correlated with the number of calcium nodules. It is consistent with the results in Fig. 9A, which illustrates the difference in the cell differentiation level on different films.

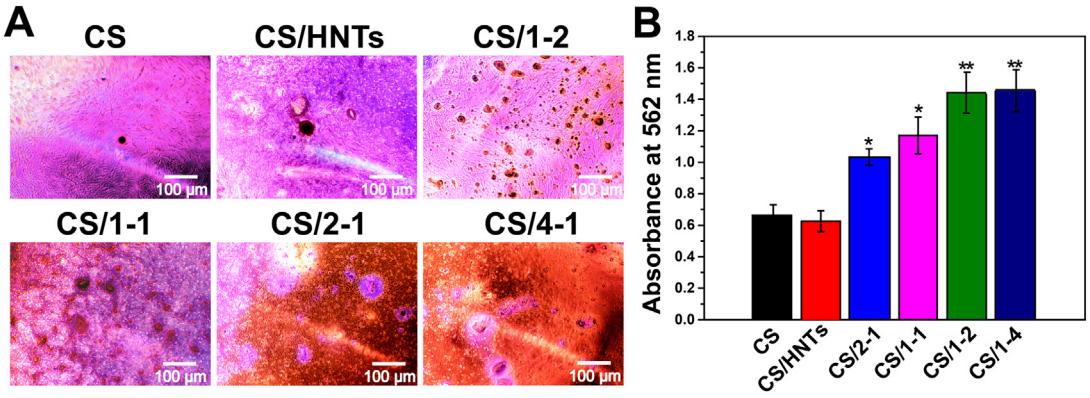

Fig. 9. The photos of ARS staining (A) and the semiquantitative result (B) of MC3T3-E1 cells culturing on films after 21 days. The results are presented as mean ± SD ($n = 24$) in 3 separate experiments. The data were analyzed by SPSS Statistic 22.0. *$P < 0.05$; **$P < 0.01$ versus CS group. (For interpretation of the references to color in this figure, the reader is referred to the web version of this article.)

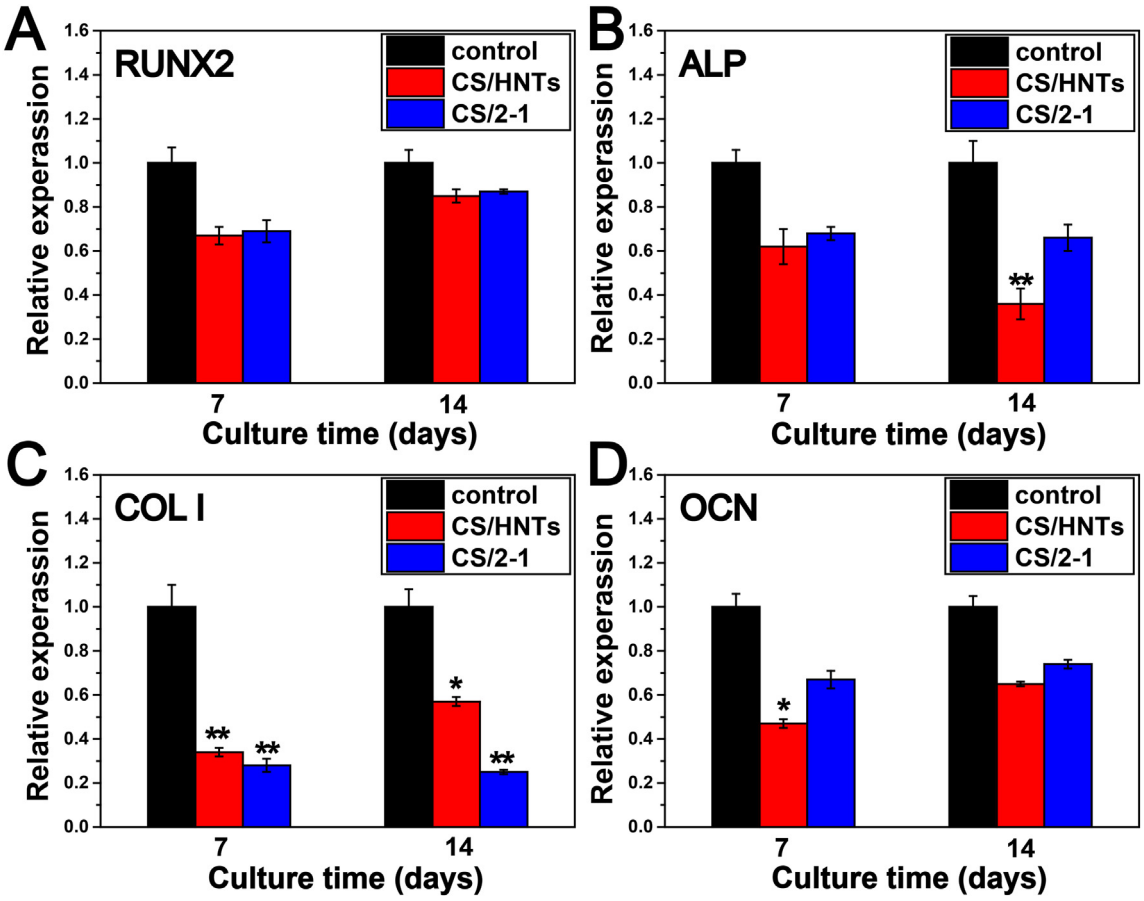

Fig. 10. qRT-PCR of osteogenic related genes expression (A: RUNX2, B: ALP, C: COL I, D: OCN) of MC3T3-E1 cells cultured on culture-plates, CS/HNTs and CS/2-1. The data were analyzed by SPSS Statistic 22.0. *$P < 0.05$; **$P < 0.01$ versus control group.

The effect of the composite films on the differentiation of MC3T3-E1 cells was further examined by qRT-PCR. The target genes for the osteogenic differentiation level are RUNX2, ALP, COL I and OCN. The level of osteogenic differentiation of the cells on the composite film is evaluated. The cells growing in the culture plate are set as a control group. During the experiment, the growth of control groups was better than that of the composite film. Thus, the relative expression of related genes on the blank groups is higher than that of the experimental groups. RUNX2 is the beginning marker of osteogenic differentiation to regulate the expression of several osteoblastic genes including COL I and OCN [58]. On day 7 and day 14, the relative expression of RUNX2 of cells on CS/HNTs and CS/2-1 is similar. Both expression levels on day 14 are higher than that of day 7 (Fig. 10A). ALP, an early marker of osteogenic differentiation, reaches its peaks at the matrix of maturing and decreases at the late stage of differentiation [59]. On day 14, the expression on CS/2-1 is still same as that of day 7 which indicates the early stages of osteogenic differentiation of cells on CS/2-1 (Fig. 10B). COL I and OCN are the late expression of osteogenic differentiation. The expression of COL I on CS/2-1 is significantly lower than the blank group ($P < 0.01$), as shown in Fig. 10C. This suggests that HAP would influence the expression of collagen. The expression of ONC on CS/2-1 is higher than that of CS/HNTs (Fig. 10D). It indicates that the

introduction of HAP on HNTs has a promoting effect on the osteogenic differentiation of cells.

4. Conclusion

HAP@HNTs were prepared by hydrothermal reaction to investigate their cytocompatibility and their influence on the properties of chitosan films. TEM and SEM results confirmed the rod-like morphology of the HAP nanoparticles on HNTs, and the dispersibility of HAP is significantly improved in aqueous solution as measured by DLS. HAP@HNTs show high specific surface area and a similar crystal structure with pure HAP. Due to the introduction of bioactive HAP, HAP@HNTs have excellent cell compatibility and osteogenic differentiation ability, which were observed by CCK-8 assay, AO/EB assays, and ALP assays. The chitosan composite film was obtained by adding HAP@HNTs into chitosan by solution mixing. HAP@HNTs can be uniformly dispersed in chitosan matrix and show high reinforcing ability towards chitosan. The cytocompatibility and osteogenic differentiation ability of the composite film evaluated by CCK-8 assays, AO/EB assays, ALP assays, ARS assays and qRT-PCR show that HAP@HNTs increases the proliferation and differentiation of MC3T3-E1 pre-osteogenic cells. Therefore, HAP@HNTs are suitable to incorporate into the biomedical polymers as functional nanoparticles. This work develops a facial synthesis method of bioactive HAP@HNTs, which shows promising application as a novel bone regeneration biomaterial as local delivery systems with improved osteoinductive properties.

Declaration of competing interest

There are no conflicts of interest to declare.

Acknowledgments

This work was financially supported by the National Natural Science Foundation of China (51473069 and 51502113), the Pearl River S&T Nova Program of Guangzhou (201610010026), and the Fundamental Research Funds for the Central Universities (21619102).

Appendix A. Supplementary data

The supporting information includes EDS spectrum of HAP and 1-1 and the survey of XPS spectra and high-resolution scanning of CS/1-1 composite film and CS film. Supplementary data to this article can be found online at doi:https://doi.org/10.1016/j.msec.2019.110072.

References

[1] M. Liu, Z. Jia, D. Jia, C. Zhou, Recent advance in research on halloysite nanotubes-polymer nanocomposite, Prog. Polym. Sci. 39 (2014) 1498–1525.
[2] M. Liu, Y. Zhang, C. Wu, S. Xiong, C. Zhou, Chitosan/halloysite nanotubes bionanocomposites: structure, mechanical properties and biocompatibility, Int. J. Biol. Macromol. 51 (2012) 566–575.
[3] N. Cai, Q. Dai, Z. Wang, X. Luo, Y. Xue, F. Yu, Toughening of electrospun poly(L-lactic acid) nanofiber scaffolds with unidirectionally aligned halloysite nanotubes, J. Mater. Sci. 50 (2015) 1435–1445.
[4] P. Yuan, D. Tan, F. Annabi-Bergaya, Properties and applications of halloysite nanotubes: recent research advances and future prospects, Appl. Clay Sci. 112 (2015) 75–93.
[5] Y.M. Lvov, D.G. Shchukin, H. Möhwald, R.R. Price, Halloysite clay nanotubes for controlled release of protective agents, ACS Nano 2 (2008) 814–820.
[6] M.J. Mitchell, C.S. Chen, V. Ponmudi, A.D. Hughes, M.R. King, E-selectin liposomal and nanotube-targeted delivery of doxorubicin to circulating tumor cells, J. Control. Release 160 (2012) 609–617.
[7] K.M. Rao, S. Nagappan, D.J. Seo, C.-S. Ha, pH sensitive halloysite-sodium hyaluronate/poly(hydroxyethyl methacrylate) nanocomposites for colon cancer drug delivery, Appl. Clay Sci. 97-98 (2014) 33–42.
[8] Y. Wu, J. Yang, H. Gao, Y. Shen, L. Jiang, C. Zhou, Y. Li, R. He, M. Liu, Folate-conjugated halloysite nanotubes, an efficient drug carrier, deliver doxorubicin for targeted therapy of breast cancer, ACS Appl. Nano Mater. 1 (2018) 595–608.
[9] Z. Long, J. Zhang, Y. Shen, C. Zhou, M. Liu, Polyethyleneimine grafted short halloysite nanotubes for gene delivery, Mater. Sci. Eng., C 81 (2017) 224–235.
[10] E. Abdullayev, Y. Lvov, Clay nanotubes for corrosion inhibitor encapsulation: release control with end stoppers, J. Mater. Chem. 20 (2010) 6681–6687.
[11] F. Tescione, G.G. Buonocore, M. Stanzione, M. Oliviero, M. Lavorgna, Controlling the release of active compounds from the inorganic carrier halloysite, International Conference on Times of Polymers & Composites, 1599 2014, pp. 446–449.
[12] M. Massaro, A. Campofelice, C.G. Colletti, G. Lazzara, R. Noto, S. Riela, Functionalized halloysite nanotubes: efficient carrier systems for antifungine drugs, Appl. Clay Sci. 160 (2018) 186–192.
[13] L. Ji, Q. Wei, Y. Zhang, H. Wu, S. Miao, Z. Cheng, Q. Gong, L. Ji, A. Zhu, A gelatin composite scaffold strengthened by drug-loaded halloysite nanotubes, Mater. Sci. Eng., C 78 (2017) 362–369.
[14] R. Shi, Y. Niu, M. Gong, J. Ye, W. Tian, L. Zhang, Antimicrobial gelatin-based elastomer nanocomposite membrane loaded with ciprofloxacin and polymyxin B sulfate in halloysite nanotubes for wound dressing, Mater. Sci. Eng., C 87 (2018) 128–138.
[15] J. Kurczewska, P. Pecyna, M. Ratajczak, M. Gajęcka, G. Schroeder, Halloysite nanotubes as carriers of vancomycin in alginate-based wound dressing, Saudi Pharm. J. 25 (2017) 911–920.
[16] M. Liu, R. He, J. Yang, W. Zhao, C. Zhou, Stripe-like clay nanotubes patterns in glass capillary tubes for capture of tumor cells, ACS Appl. Mater. Inter. 8 (2016) 7709–7719.
[17] G.I. Fakhrullina, F.S. Akhatova, Y.M. Lvov, R.F. Fakhrullin, Toxicity of halloysite clay nanotubes *in vivo*: a Caenorhabditis elegans study, Environ. Sci. Nano 2 (2015) 54–59.
[18] X. Wang, J. Gong, Z. Gui, T. Hu, X. Xu, Halloysite nanotubes-induced Al accumulation and oxidative damage in liver of mice after 30-day repeated oral administration, Environ. Toxicol. 33 (2018) 623–630.
[19] Z. Long, Y. Wu, H. Gao, J. Zhang, X. Ou, R. He, M. Liu, *In vitro* and *in vivo* toxicity evaluation of halloysite nanotubes, J. Mater. Chem. B 6 (2018) 7204–7216.
[20] M.D. Paola, A. Quarta, P. Pisani, F. Conversano, E.A. Sbenaglia, S. Leporatti, G. Gigli, S. Casciaro, Surface coating highly improves cytocompatibility of halloysite nanotubes: a metabolic and ultrastructural study, IEEE T. Nanotechnol. 15 (2016) 770–774.
[21] J. Zhang, T. Liu, M. Liu, Hydrothermal synthesis of halloysite nanotubes@carbon nanocomposites with good biocompatibility, Micropor. Mesopor. Mater. 266 (2018) 155–163.
[22] S. Feng, R. Xu, New materials in hydrothermal synthesis, Acc. Chem. Res. 34 (2001) 239–247.
[23] R.Z. Legeros, Properties of osteoconductive biomaterials: calcium phosphates, Clin. Orthop. Relat. Res. 395 (2002) 81–98.
[24] R. Zhang, P.X. Ma, Poly (α-hydroxyl acids)/hydroxyapatite porous composites for bone-tissue engineering. I. Preparation and morphology, J. Biomed. Mater. Res. 44 (1999) 446–455.
[25] W. Suchanek, M. Yoshimura, Processing and properties of hydroxyapatite-based biomaterials for use as hard tissue replacement implants, J. Mater. Res. 13 (1998) 94–117.
[26] T. Noriyuki, M. Akira, T. Tetsuya, N. Takanobu, T. Junzo, O. Takahiro, Y. Hideki, Novel hydroxyapatite ceramics with an interconnective porous structure exhibit superior osteoconduction *in vivo*, J. Biomed. Mater. Res. 59 (2002) 110–117.
[27] F. Valenzuela, C. Covarrubias, C. Martínez, P. Smith, M. Díaz-Dosque, M. Yazdani-Pedram, Preparation and bioactive properties of novel bone-repair bionanocomposites based on hydroxyapatite and bioactive glass nanoparticles, J. Biomed. Mater. Res., Part B 100 (2012) 1672–1682.
[28] G. Wei, P.X. Ma, Structure and properties of nano-hydroxyapatite/polymer composite scaffolds for bone tissue engineering, Biomaterials 25 (2004) 4749–4757.
[29] F. Sun, H. Zhou, J. Lee, Various preparation methods of highly porous hydroxyapatite/polymer nanoscale biocomposites for bone regeneration, Acta Biomater. 7 (2011) 3813–3828.
[30] P. Habibovic, F. Barrère, C.A.V. Blitterswijk, K.D. Groot, P. Layrolle, Biomimetic hydroxyapatite coating on metal implants, J. Am. Ceram. Soc. 85 (2010) 517–522.
[31] S. Wang, X. Wang, H. Xu, H. Abe, Z. Tan, Y. Zhao, J. Guo, M. Naito, H. Ichikawa, Y. Fukumori, Towards sustained delivery of small molecular drugs using hydroxyapatite microspheres as the vehicle, Adv. Powder Technol. 21 (2010) 268–272.
[32] K. Tomoda, H. Ariizumi, T. Nakaji, K. Makino, Hydroxyapatite particles as drug carriers for proteins, Colloids Surf., B 76 (2010) 226–235.
[33] I. Sopyan, M. Mel, S. Ramesh, K.A. Khalid, Porous hydroxyapatite for artificial bone applications, Sci. Technol. Adv. Mater. 8 (2007) 116–123.
[34] H. Sun, M. Jiang, S. Zhu, *In vitro* and *in vivo* studies on hydroxyapatite nanoparticles as a novel vector for inner ear gene therapy, Chinese Journal of Otorhinolaryngology Head and Neck Surgery 43 (2008) 51–57.
[35] G. Wang, Y. Zhao, J. Tan, S. Hong, K. Zhou, Arginine functionalized hydroxyapatite nanoparticles and its bioactivity for gene delivery, T. Nonferr. Metal. Soc. 25 (2015) 490–496.
[36] K. Loku, G. Kawachi, S. Sasaki, H. Fujimori, S. Goto, Hydrothermal preparation of tailored hydroxyapatite, J. Mater. Sci. 41 (2006) 1341–1344.
[37] S.J. Eppell, W. Tong, J.L. Katz, L. Kuhn, M.J. Glimcher, Shape and size of isolated bone mineralites measured using atomic force microscopy, J. Orthop. Res. 19 (2010) 1027–1034.
[38] H.S. Gupta, S. Jong, W. Wolfgang, Z. Paul, B. Peter, F. Peter, Cooperative deformation of mineral and collagen in bone at the nanoscale, PNAS 103 (2006) 17741–17746.
[39] I. Deen, X. Pang, I. Zhitomirsky, Electrophoretic deposition of composite chitosan–halloysite nanotube–hydroxyapatite films, Colloids Surf. A Physicochem. Eng. Asp. 410 (2012) 38–44.
[40] I. Deen, I. Zhitomirsky, Electrophoretic deposition of composite halloysite nanotube–hydroxyapatite–hyaluronic acid films, J. Alloys Compd. 586 (2014)

S531–S534.
[41] J. Zhang, L. Fan, A. Wang, *In situ* generation of sodium alginate/hydroxyapatite/halloysite nanotubes nanocomposite hydrogel beads as drug-controlled release matrices, J. Mater. Chem. B 1 (2013) 6261–6270.
[42] M. Liu, B. Guo, Q. Zou, M. Du, D. Jia, Interactions between halloysite nanotubes and 2,5-bis(2-benzoxazolyl) thiophene and their effects on reinforcement of polypropylene/halloysite nanocomposites, Nanotechnology 19 (2008) 205709.
[43] H. Zhang, K. Zhou, Z. Li, S. Huang, Plate-like hydroxyapatite nanoparticles synthesized by the hydrothermal method, J. Phys. Chem. Solids 70 (2009) 243–248.
[44] K. Jiang, A. Eitan, L.S. Schadler, P.M. Ajayan, R.W. Siegel, Selective attachment of gold nanoparticles to nitrogen-doped carbon nanotubes, Nano Lett. 3 (2003) 275–277.
[45] G.A. Rance, D.H. Marsh, S.J. Bourne, T.J. Reade, A.N. Khlobystov, van der Waals interactions between nanotubes and nanoparticles for controlled assembly of composite nanostructures, ACS Nano 4 (2010) 4920–4928.
[46] W. Xing, N. Liang, P. Huo, Z. Lu, X. Liu, Y. Luo, Y. Yan, Preparation high photocatalytic activity of CdS/halloysite nanotubes (HNTs) nanocomposites with hydrothermal method, Appl. Surf. Sci. 259 (2012) 698–704.
[47] F. Abbona, A. Baronnet, A XRD and TEM study on the transformation of amorphous calcium phosphate in the presence of magnesium, J. Cryst. Growth 165 (1996) 98–105.
[48] J. Klinkaewnarong, E. Swatsitang, S. Maensiri, Nanocrystalline hydroxyapatite powders by a chitosan–polymer complex solution route: synthesis and characterization, Solid State Sci. 11 (2009) 1023–1027.
[49] B. Wang, W. Zhang, W. Zhang, A.S. Mujumdar, L. Huang, Progress in drying technology for nanomaterials, Dry. Technol. 23 (2005) 7–32.
[50] A.M. Carrillo, J.G. Carriazo, Cu and Co oxides supported on halloysite for the total oxidation of toluene, Appl. Catal., B 164 (2015) 443–452.
[51] B. Huang, M. Liu, C. Zhou, Chitosan composite hydrogels reinforced with natural clay nanotubes, Carbohyd. Polym. 175 (2017) 689–698.
[52] H. Alobeedallah, J.L. Ellis, R. Rohanizadeh, H. Coster, F. Dehghani, Preparation of nanostructured hydroxyapatite in organic solvents for clinical applications, Trends Biomater. Artif. Organs 25 (2011) 12–19.
[53] B. Priyadarshini, U. Anjaneyulu, U. Vijayalakshmi, Preparation and characterization of sol-gel derived Ce^{4+} doped hydroxyapatite and its *in vitro* biological evaluations for orthopedic applications, Mater. Design 119 (2017) 446–455.
[54] G.W. Brindley, K. Robinson, D.M.C. Macewan, The clay minerals halloysite and meta-halloysite, Nature 157 (1946) 225–226.
[55] R. Kam, C. Selomulya, R. Amal, J. Scott, The influence of La-doping on the activity and stability of Cu/ZnO catalyst for the low-temperature water–gas shift reaction, J. Catal. 273 (2010) 73–81.
[56] S.-S. Kim, M.S. Park, O. Jeon, C.Y. Choi, B.-S. Kim, Poly (lactide-co-glycolide)/hydroxyapatite composite scaffolds for bone tissue engineering, Biomaterials 27 (2006) 1399–1409.
[57] M. Liu, C. Wu, Y. Jiao, S. Xiong, C. Zhou, Chitosan–halloysite nanotubes nanocomposite scaffolds for tissue engineering, J. Mater. Chem. B 1 (2013) 2078–2089.
[58] L. Gilbert, X. He, P. Farmer, J. Rubin, H. Drissi, A.J.V. Wijnen, J.B. Lian, G.S. Stein, M.S. Nanes, Expression of the osteoblast differentiation factor RUNX2 (Cbfa1/AML3/Pebp2αA) is inhibited by tumor necrosis factor-α, J. Biol. Chem. 277 (2002) 2695–2701.
[59] L. Lecoeur, J.P. Ouhayoun, *In vitro* induction of osteogenic differentiation from non-osteogenic mesenchymal cells, Biomaterials 18 (1997) 989–993.